Nucleation site potency distributions in thermoelastic martensitic transformation in $Ni_{43}Co_7Mn_{39}Sn_{11}$ particles

Yijia Zhang, Carlos Lago, Ibrahim Karaman, and Patrick J. Shamberger*
Department of Materials Science and Engineering, Texas A&M University, College Station, Texas 77843, USA

(Received 1 September 2020; revised 23 December 2020; accepted 14 January 2021; published 22 February 2021)

The relationship between the nucleation process and thermal hysteresis width in reversible thermoelastic martensitic transformations remains unclear, particularly as the volume of transforming material decreases. Understanding the number density and nature of defects which serve as nucleation sites in this class of materials requires a quantitative analysis of nucleation site potency distributions in different classes of materials with different intrinsic barriers to nucleation. Here, we investigate the size dependence of hysteresis in microscale $Ni_{43}Co_7Mn_{39}Sn_{11}$ alloy particles (radius 4.4–19.0 μm) during reversible martensitic transformations by collecting temperature-dependent magnetization of 126 individual alloy particles. Size-dependent hysteresis is quantified by a power law model and attributed to friction-induced energy dissipation. In samples with ideal nucleation-limited transformations, martensitic transformation temperatures on cooling decreased with decreasing particle volume due to the low probability of including relatively sparse high-energy nucleation sites. Nucleation site potency distributions are quantified as a function of thermodynamic driving force and compared against potency distributions for thermoelastic martensitic transformations in other classes of materials and for burst martensitic transformations. Across different classes of materials, as the energy barrier associated with the martensitic transformation increases, number densities of defects with sufficient potency to nucleate the transformation decrease dramatically. This finding suggests that very different kinds of defects may be responsible for nucleation of martensitic phase transformations in different material systems.

DOI: 10.1103/PhysRevMaterials.5.023401

I. INTRODUCTION

Understanding the origins of size dependence in martensitic transformations improves the possibility of controlled transformation temperatures, widths, and hysteresis for various applications (e.g., shape-memory actuators [1] and caloric effect refrigeration [2–4]) and, in particular, for micro- and nanoscale multifunctional devices [5,6]. As an example, small diameter multifunctional alloy particles, wires, or films with relatively large surface to volume ratios have improved heat transfer rates, resulting in close to isothermal transformations, thereby increasing the efficiency of heat pump cycles based on caloric effect materials [2,4,7,8]. Thermoelastic martensitic transformations, which have a low-energy barrier to transformation, nucleate from sparse high-energy nucleation sites, followed by domain growth until local thermal and elastic equilibria in the system are reached [9–11]. For reversible thermoelastic martensitic transformations in small volumes of material, nucleation of the first domain can represent the critical rate-limiting step, after which mobile austenite/martensite interfaces propagate rapidly through the sample volume [11,12]. While intrinsic nucleation site populations have been critically analyzed for burst martensite systems which have relatively larger barriers to phase transformation [12–14], the relationship between defect populations and their potency as potential nucleation sites is anticipated to behave very differently in thermoelastic martensitic systems due to the much lower strain energy barrier. Thus, in order to understand the correlation between the magnitude of the strain energy barrier and nucleation site populations, we are motivated to quantify and compare nucleation site potency in thermoelastic martensitic systems.

Reducing the characteristic length scale of an alloy volume undergoing a martensitic transformation impacts transformation temperatures, stresses, and hysteresis by introducing additional surface and interfacial area and by decreasing the number of potential nucleation sites available to initiate martensitic phase transformations [9,12,15,16]. With decreasing grain size to sample dimension ratios, martensite start stress and stress hysteresis increased in Cu-based shape-memory alloy wire, bars, and sheets [17–20]. This phenomenon has been attributed to enhanced barrier effects due to dislocation pileup at grain boundaries in small grains [21]. Nonhysteretic superelasticity of nanoscale shape-memory alloys has been studied by molecular dynamics simulations [22]. With applied stress, the martensitic transformation occurred without sudden nucleation due to the disappearance of the energy barrier between the cubic parent phase and orthorhombic martensite when the particle diameter decreased to 2.0 nm [22]. Stress hysteresis and thermal hysteresis both increased in thinner Cu-Al-Ni alloy microwires during thermoelastic martensitic transformations [15]. Similarly, thermal hysteresis increased with decreasing film thicknesses and increasing surface area to volume ratios in microscale Ni-Mn-Sn alloy films [16]. In all of these cases, the size-dependent

*patrick.shamberger@tamu.edu

hysteresis is primarily attributed to an interaction between the mobile martensite/austenite interface, and defects at the alloy/substrate interface or free surface, resulting in friction-induced energy dissipation, which increases with increasing surface area to volume ratios [9,15,16].

Hysteresis in micro- and nanoscopic volumes of alloys with nucleation-limited transformations is dependent on the potency of the defect sites, which serve to nucleate the forward and reverse transformations [5,23]. In the seminal study of the process of irreversible burst martensitic transformations upon cooling of microscale Fe-Ni alloy particles (diameter $\leqslant$ 105 μm), the fraction of transformed particles decreased with decreasing particle volume due to the decreased probability of including relatively sparse high-energy nucleation sites within a given volume [12]. Contrasting against gradual stress-strain curves of bulk Cu-Al-Ni single crystals, abrupt and discontinuous stress-strain curves were dominated by nucleation controlled behavior in submicrometer Cu-Al-Ni pillars (diameter <2 μm) during thermoelastic martensitic transformations [24,25]. The lack of nucleation sites in these pillars served as a barrier to the stress-induced martensitic transformations, resulting in large hysteresis. Similarly, Ni-Fe-Ga shape-memory alloy pillars (diameter <10 μm) with a smaller diameter presented a lower martensite start temperature [23]. When the size of the sample was reduced to a critical value (50 nm thickness for films or 60 nm diameter for grains), the martensitic transformations were suppressed in nanoscale Ni-Ti alloy films and nanocrystals [26,27]. In all of these cases, the volume of material transforming was small enough that the occurrence of highly potent nucleation sites was statistically improbable, resulting in a larger transformation hysteresis than observed in larger particles.

Various defects have been shown to be effective as nucleation sites by *in situ* observation using transmission electron microscopy [28–33]. Martensite nucleated at the intersection between shear bands, from active slip planes, along grain boundaries, and at triple junctions, which were believed to provide favorable nucleation sites in strain-induced burst martensitic transformations in Fe alloys [28–31]. During thermoelastic martensitic transformations in Ti-Ni-Cu alloys, very early stages of martensite formed at a stress field near dislocation tangles or a stress concentration at the surface [32]. During reversible martensitic transformations in Au-Cd alloys, martensite emanated from grain boundaries and associated dislocation arrays, followed by propagation of individual martensite plates across grain boundaries or into the untransformed regions [33]. However, comprehensive measurement of nucleation site populations by electron microscopy is intractable due to the sparse nature of nucleation sites and the possibility of introducing new defects during the preparation of thin foils for electron microscopy. A statistical approach that can quantitatively analyze nucleation site potency distribution is required in order to establish correlations between heterogeneous nucleation sites and sparse defects in martensitic transformation systems.

Here, we study reversible thermoelastic martensitic transformations in microscale spherical $Ni_{43}Co_7Mn_{39}Sn_{11}$ particles ($4.4 \leqslant r \leqslant 19.0$ μm) synthesized by gas atomization. Temperature-dependent magnetization curves of individual single-crystal particles are used to classify phase transformation behavior on the basis of the degree of abruptness of the transformation during both cooling and heating. With decreasing particle size and volume, the hysteresis of alloy particles increased. For particles with gradual phase transformations, size-dependent hysteresis is quantified by a power law model and attributed to friction-induced energy dissipation. For particles with hybrid and abrupt phase transformations, which are identified as nucleation-limited transformations, nucleation site potency distributions are quantified as a function of thermodynamic driving force and compared against other martensitic transformation materials. With increasing thermodynamic driving force, nucleation site densities in $Ni_{43}Co_7Mn_{39}Sn_{11}$ particles increase with similar tendency to that observed previously in other thermoreversible transformations, although with a much greater absolute number density for a particular thermodynamic driving force.

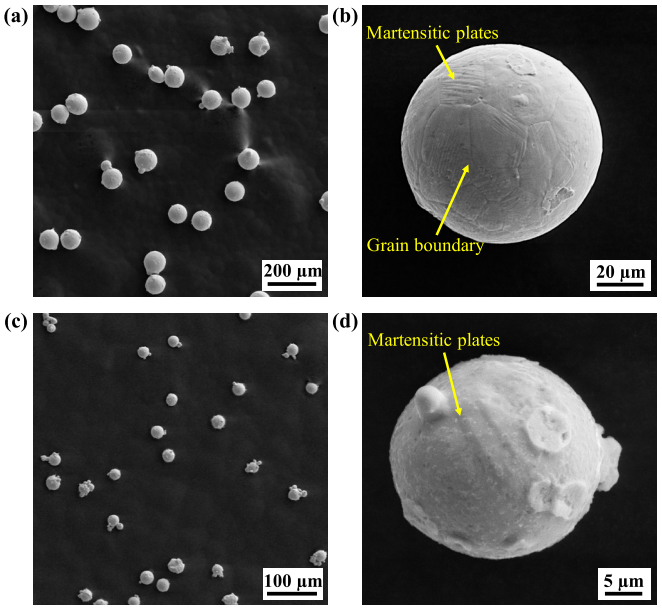

FIG. 1. Shape of $Ni_{43}Co_7Mn_{39}Sn_{11}$ particles from groups with radius (a) 37.5–45 μm and (c) 12.5–16 μm, and examples of individual particle, (b) $r = 43.5 \pm 0.5$ μm and (d) $r = 14.3 \pm 0.5$ μm under SEM.

II. METHODS

Spherical $Ni_{43}Co_7Mn_{39}Sn_{11}$ (at.%) particles were fabricated from the melt by nitrogen gas atomization [34]. The as-received particles were sealed in a quartz tube in an argon (purity 99.999%) atmosphere, heated to 1173 K at 30 K/min, annealed for 12 h to promote chemical homogenization, and then furnace cooled. The annealed particles were sieved by a vibratory sieve shaker using 90–20 μm diameter Gilson acrylic frame sieves and 15–10 μm diameter Advantech precision sonic sifter sieves.

With decreasing particle radius, the microstructure of particles changed from polycrystals to single crystals. Eighty-eight percent of particles in Fig. 1(a) and 59% of particles in Fig. 1(c) were globular with an average circularity of 0.80 by a two-dimensional (2D) image analysis of 35 particles in Fig. 1. The remaining particles were composed of small

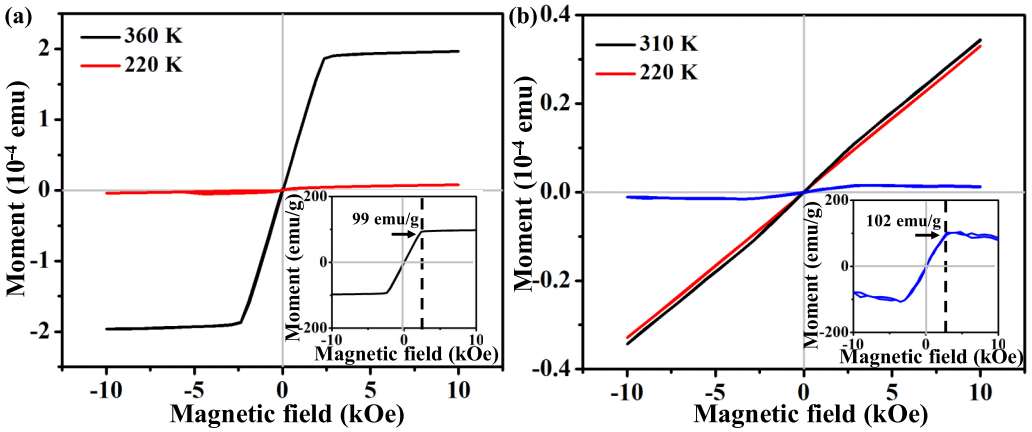

FIG. 2. $M(H)$ hysteresis loops of (a) polycrystalline particle ($r = 39.2 \pm 0.5$ μm, 2.1×10^{-6} g) and (b) single-crystal particle ($r = 7.7 \pm 0.5$ μm, 1.6×10^{-8} g) at both high temperatures (austenite, black line) and low temperatures (martensite, red line), the inset represents the $M(H)$ hysteresis loop of the single-crystal particle at 310 K after removing the background signal.

agglomerated clusters. For polycrystalline particles, grain boundaries and martensitic plates were visible at the surface in scanning electron microscopy (SEM) and optical microscopy images [Fig. 1(b)]. Small particles (<38 μm diameter) did not show grain boundaries at the surface and were identified as single crystals [Fig. 1(d)].

Differential scanning calorimetry (DSC) was performed on a TA Q2000 with 10 K/min heating and cooling rates under a nitrogen atmosphere. Scanning electron Microscopy (SEM) was performed on a Tescan Lyra-3 at 20 keV accelerating voltage (secondary electron imaging). An individual $Ni_{43}Co_7Mn_{39}Sn_{11}$ particle was picked up by a small piece of polyimide (Kapton) tape with silicone adhesive as the sample for magnetization measurements. A BX53M Olympus upright microscope was used to inspect the tape for contamination and to take pictures of each particle for analyzing particle radius (Fig. S1, Supplemental Material [35]). Particle radius was measured using IMAGEJ software. The mass of each alloy particle is calculated by multiplying volume by the estimated alloy density (8.3 g/cm^3) [36]. Magnetic properties were evaluated on a superconducting quantum interference device magnetometer under vibrating sample magnetometer mode (Quantum Design MPMS 3 with sensitivity $<1 \times 10^{-8}$ emu when the magnetic field is smaller than 2.5 kOe, and $<8 \times 10^{-8}$ emu when the magnetic field is larger than 2.5 kOe).

With decreasing particle volume, the signal to noise ratio of the $M(T)$ curves decreases. $M(T)$ curves of 126 individual single-crystal particles ($4.4 \leqslant r \leqslant 19.0$ μm) were obtained under 5 kOe with 5 K/min heating and cooling rates. Due to the limitation of the instrument sensitivity, the smallest particle which has been tested and displays a measurable $M(T)$ curve has a radius of $r = 4.4 \pm 0.5$ μm (Fig. S2 [35]). In the smallest particles, it is difficult to clearly assign austenite start and finish (A_s, A_f) and martensite start and finish (M_s, M_f) temperatures due to the strong noise. Thus we use a straight line, which is parallel and in the middle of two tangent lines, to find the point of intersection during heating (cooling), and record the X-axis value as $(A_s + A_f)/2$ during heating and $(M_s + M_f)/2$ during cooling (Fig. S2 [35]). The difference of temperature between $(A_s + A_f)/2$ and $(M_s + M_f)/2$ is recorded as thermal hysteresis width [$\Delta T_{hyst} = (A_s + A_f)/2$–$(M_s + M_f)/2$].

III. RESULTS

A. Soft ferromagnetic alloy particles

$Ni_{43}Co_7Mn_{39}Sn_{11}$ small particles are soft ferromagnets at 360 K (austenite);they saturate at magnetic fields of approximately 3 kOe (Fig. 2). In the martensite phase, $Ni_{43}Co_7Mn_{39}Sn_{11}$ alloy particles show a very low magnetization [Fig. 2(a)]. Very low magnetization has been observed in Ni-Co-Mn-In alloys (low-temperature martensitic phase), as well as in other Ni-Mn-X alloy families, where it has generally been attributed to the existence of antiferromagnetic correlations in the martensite phase [37–39]. For very small particles ($r < 5$ μm), the magnetic signal from the particle approaches the instrument's noise floor, and is small relative to the total magnetic signal measured [which includes non-negligible paramagnetic or diamagnetic signal from sample holder, mounts, and any potential contaminants, that vary slightly from sample to sample; see Fig. 2(b)]. However, the $M(H)$ hysteresis loops of a blank sample (including a sample mount but no particle) remain nearly temperature independent over the temperature range 220–360 K (Fig. S3, Supplemental Material [35]). Therefore, we remove the background signal by subtracting the magnetization at 220 K (martensite) from the magnetization at higher temperatures [Fig. 2(b)], resulting in a magnetic difference signal $\Delta M_H(T) = M_H(T)$–$M_H(220\ K)$. This signal is a sensitive measure of the internal state of a particle. The $\Delta M_H(T)$ curve of the single-crystal particle ($r = 7.7 \pm 0.5$ μm) shows the same soft ferromagnetic behavior as the polycrystalline particle ($r = 39.2 \pm 0.5$ μm) in the austenite phase (Fig. 2, insets).

To evaluate the validity of this approach, we compare the measured $\Delta M(M_{austenite}$–$M_{220\ K})$ of individual particles with the calculated ΔM on the basis of particle volume. ΔM is measured with a magnetic field of 5 kOe, because at this field, particles are saturated and show similar thermal hysteresis widths of $\Delta M(T)$ curves. Details are discussed in Sec. III D. The ΔM's of small particles are proportional to their volume

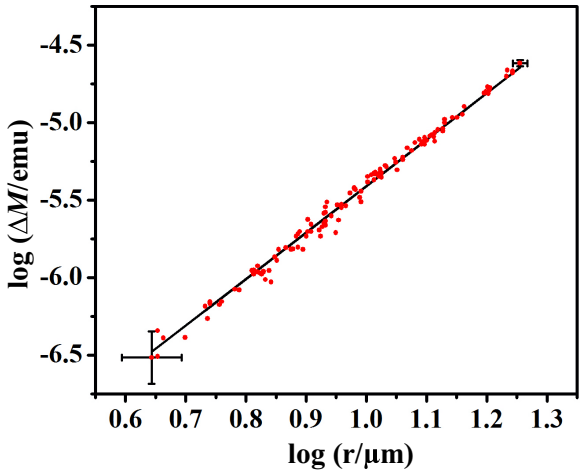

FIG. 3. Distribution of measured ΔM against particle radius (red dot), and the expected relationship based on ΔM of 116.5 emu/g measured in a large particle ($r = 39.5 \pm 0.5$ μm, black line). Uncertainties are labeled on the smallest and the largest alloy particles based on the measurement accuracy of particle magnetization and radius.

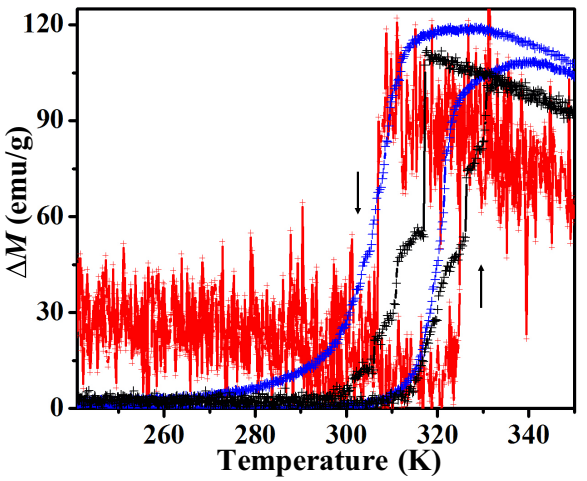

FIG. 4. $\Delta M(T)$ curves of an alloy particle with an abrupt transformation ($r = 6.2 \pm 0.5$ μm, red line), with a hybrid transformation ($r = 13.4 \pm 0.5$ μm, black line), and with a gradual transformation ($r = 10.8 \pm 0.5$ μm, blue line) during both cooling and heating under 5 kOe with 5 K/min heating and cooling rates.

(Fig. 3), suggesting that the extent of phase transformation in large particles and small particles is almost the same.

B. Phase transformation behavior of individual alloy particles

The martensitic phase transformation of individual single-crystal particles, as measured by $\Delta M(T)$ curves, shows different temperature-dependent transformation behavior (classified as abrupt, hybrid, or gradual transformations; see Table I and Fig. 4) based on the extent of transformation which takes place during each measurement temperature interval. Abrupt transformations are defined as taking less than 12 s, three data points, and 1 K to progress to a completion greater than 90% of the volume transformed. For a gradual transformation process, there is no discernible nucleation event, and it takes at least 3 min, 45 data points, and 15 K for an alloy particle to transform phase during cooling or heating. When transformation processes do not meet the criteria defined for abrupt or gradual transformations, the transformations are classified as hybrid. In many cases, hybrid transformations have discernible nucleation events on cooling, but these do not progress to completion (Fig. 4). By comparing the fraction of particles with abrupt and hybrid transformations during cooling and heating, the particles are more likely to nucleate during cooling.

TABLE I. The fraction of particles with abrupt, hybrid, or gradual martensitic phase transformations during cooling and heating ($N_{\text{total}} = 126$).

Heating	Abrupt	Cooling hybrid	Gradual
Abrupt	0.040	0	0
Hybrid	0.055	0.127	0
Gradual	0.008	0.127	0.643

C. Repeated cycling and rate dependence

It is informative to assess the distribution of transformation temperatures in both abrupt and gradual transformations (Fig. 5, and Fig. S4 in the Supplemental Material [35]). Thermal hysteresis widths of repeated $\Delta M(T)$ cycling of individual particles with abrupt or gradual transformations show small variations, while the hysteresis width of individual particles increases slightly with decreasing cooling and heating rates at 5 kOe external field for particles with abrupt and hybrid transformations. Repeated $\Delta M(T)$ cycling of four individual particles is performed at 5 K/min (Figs. 5(a) and 5(b), and Figs. S4(a) and S4(b) in the Supplemental Material [35]). For particles with radius 9.1, 12.6, and 14.2 μm, the variance of hysteresis width is 0.55, 0.22, and 1.03 K^2, respectively (Fig. 5(a), and Figs. S4(a) and S4(b) [35]). For the particle with gradual transformation, the hysteresis remains constant during repeated $\Delta M(T)$ cycling [Fig. 5(b)].

$\Delta M(T)$ curves of these particles with abrupt and hybrid transformations show increased hysteresis when the cooling and heating rate decreases from 5 to 1 K/min (Fig. 5(c), and Figs. S4(c) and (S4d) in the Supplemental Material [35]). This phenomenon is opposite to the anticipated rate dependence of hysteresis, suggesting that thermal gradients in the measurement system are not a significant factor [15,40]. A similar phenomenon which describes the increase of hysteresis at the lower loading rate has been reported in Cu-Al-Ni alloy micropillars, which could be explained in part by the effects of loading rates on nucleation kinetics [41]. However, it should be noted that it is difficult to discern the observed effect of ramp rate on thermal hysteresis width since it is the same order of magnitude as the cycle to cycle variance. For the particle with gradual transformation, the hysteresis does not change significantly with decreasing rates, with the only obvious rate-dependent portions being limited to the initial onset of the transformation on cooling [Fig. 5(d)].

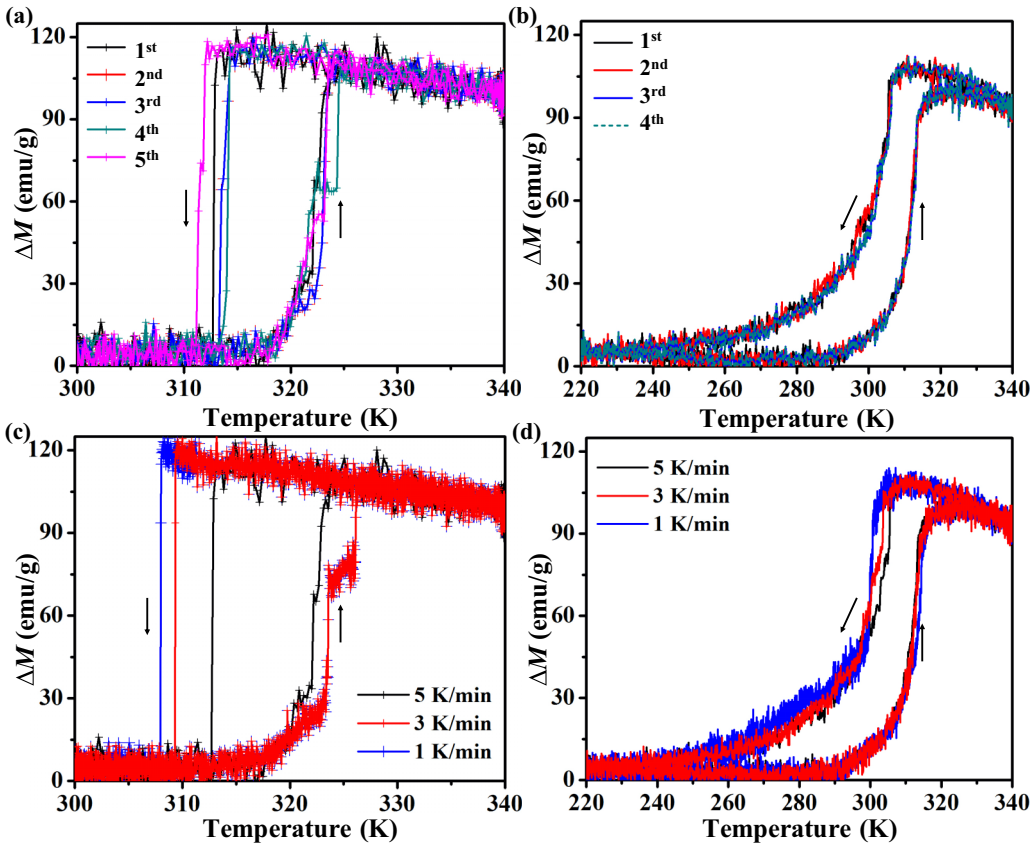

FIG. 5. (a) Repeated $\Delta M(T)$ cycling of a particle ($r = 9.1 \pm 0.5$ μm, 2.6×10^{-8} g) at 5 K/min rate; (b) repeated $\Delta M(T)$ cycling of a particle ($r = 10.4 \pm 0.5$ μm, 3.9×10^{-8} g) at 5 K/min rate; (c) $\Delta M(T)$ curves of the particle in (a) at 5, 3, 1 K/min rates, and (d) $\Delta M(T)$ curves of the particle in (b) at 5, 3, 1 K/min rates. All magnetizations measured at 5 kOe external field.

D. Magnetization measurements under different magnetic fields

Thermal hysteresis widths of $\Delta M(T)$ curves of individual alloy particles are independent of applied magnetic fields between 2 and 10 kOe based on the observation of three individual alloy particles with abrupt or gradual transformations (Fig. 6). The $\Delta M(T)$ curves of three individual alloy particles are measured between 200 and 370 K with a cooling and heating rate of 5 K/min under a series of constant magnetic fields [Figs. 6(a), 6(c), and 6(e)]. When the magnetic fields are larger than 2 kOe, the alloy particles are almost saturated and their A_s, A_f, M_s, and M_f temperatures are similar with increasing magnetic fields for the large polycrystalline particle ($r = 39.5 \pm 0.5$ μm) and the small single-crystal particle ($r = 11.5 \pm 0.5$ μm) with gradual transformations [Figs. 6(b) and 6(d)]. For the case of the single-crystal particle ($r = 12.6 \pm 0.5$ μm) with abrupt phase transformation during cooling, M_s, M_f, and A_f temperatures shift to lower temperatures when magnetic fields increase from 5 to 10 kOe [Fig. 6(f)]. When the magnetic fields are 2, 5, or 10 kOe, the variance of the thermal hysteresis width of these particles with radius 39.5, 11.5, and 12.6 μm is 0.63, 0.06, and 0.89 K^2, respectively. Thus, increasing the magnetic field will not significantly impact the thermal hysteresis width of alloy particles when the particle saturates.

IV. DISCUSSION

A. Comparing abrupt and gradual phase transformations

Abrupt phase transformations of alloy particles are consistent with nucleation-limited transformations, while gradual phase transformations are consistent with continuous nucleation and growth. Following nucleation of the first domain, abrupt phase transformations proceed to near completion within a few increments (<12 s, <1 K). On the other hand, complete gradual phase transformations occurred over more than 15 K (Fig. 7). Hybrid transformation processes consisted of both discrete nucleation events, followed by continuous growth of the nucleus and secondary nucleation events. Most of the particles showed hybrid and gradual transformations during heating (Table I). Among those particles which showed abrupt transformation during cooling, only about 37% show abrupt transformation during heating (Table I). In most hybrid transformations, the transformation from austenite to martensite started abruptly, while the transformation from martensite to austenite started gradually (Fig. 4). This is consistent with general observations of thermoelastic phase transformations in bulk polycrystalline alloys, where the cooling transition generally occurs by nucleation and growth of martensite plates, whereas the heating transition occurs by reverse growth (shrinking) of martensite plates from regions of residual trapped austenite. Similarly, residual austenite could

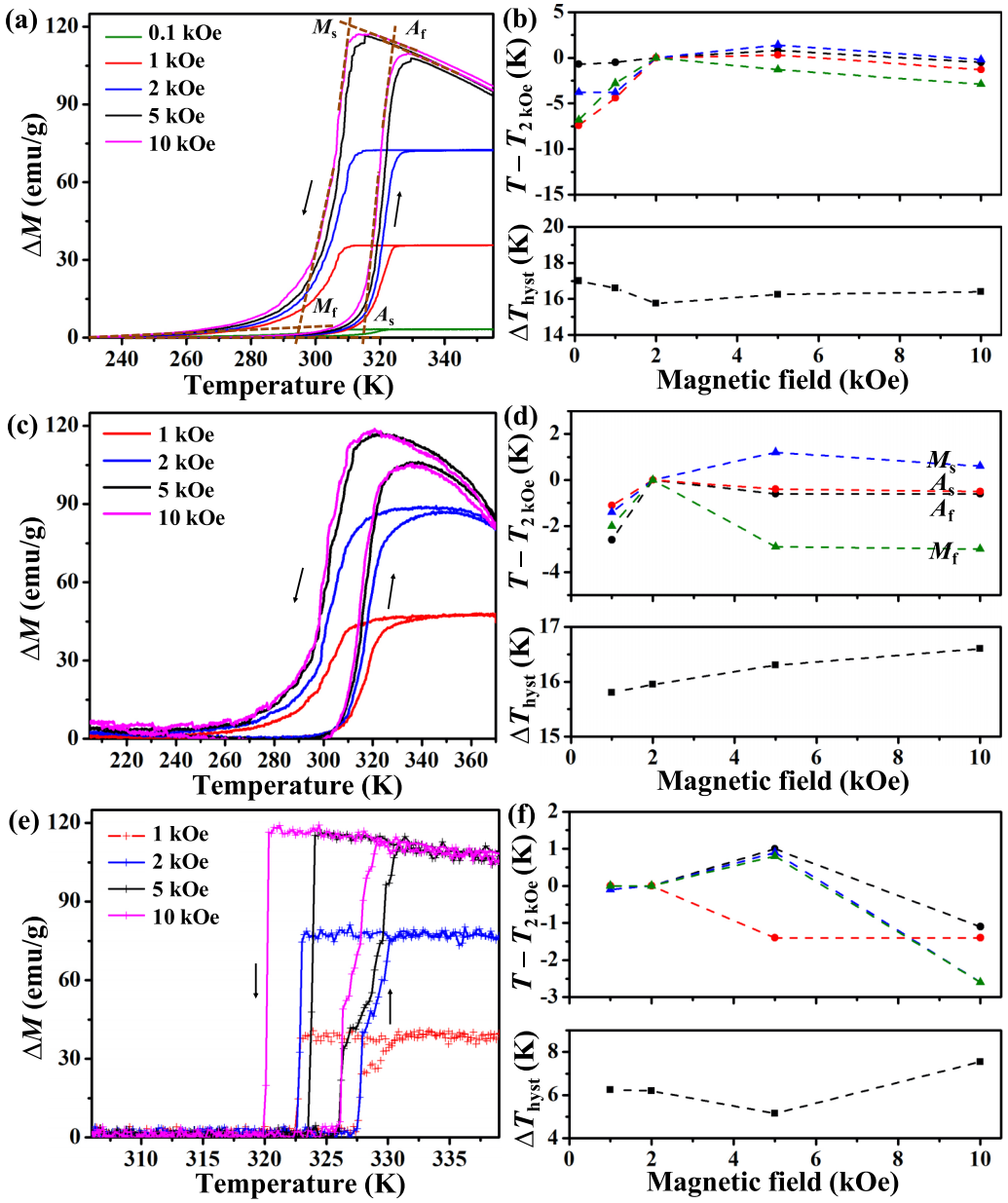

FIG. 6. $\Delta M(T)$ curves of (a) a polycrystalline particle ($r = 39.5 \pm 0.5\ \mu$m, 2.1×10^{-6} g), (c) a single-crystal particle ($r = 11.5 \pm 0.5\ \mu$m, 5.3×10^{-8} g) with gradual transformation, and (e) a single-crystal particle ($r = 12.6 \pm 0.5\ \mu$m, 7.0×10^{-8} g) with abrupt transformation during cooling under a series of magnetic fields. In (b), (d), (f), the phase transformation temperature difference, T–$T_{2\,kOe}$, and thermal hysteresis width of $\Delta M(T)$ curves in (a), (c), (e) are plotted against magnetic fields.

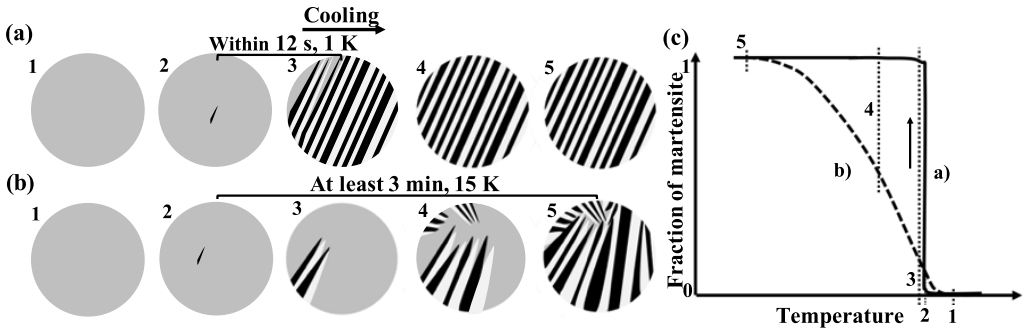

FIG. 7. Schematic diagrams of (a) abrupt martensite phase transformation and (b) gradual martensite phase transformation during cooling; (c) fraction of martensite of abrupt phase transformation (solid line) and gradual phase transformation (dashed line) during cooling. Microstructure illustrated in (a,b) inferred from the gradual or steplike character observed in $\Delta M(T)$ curves.

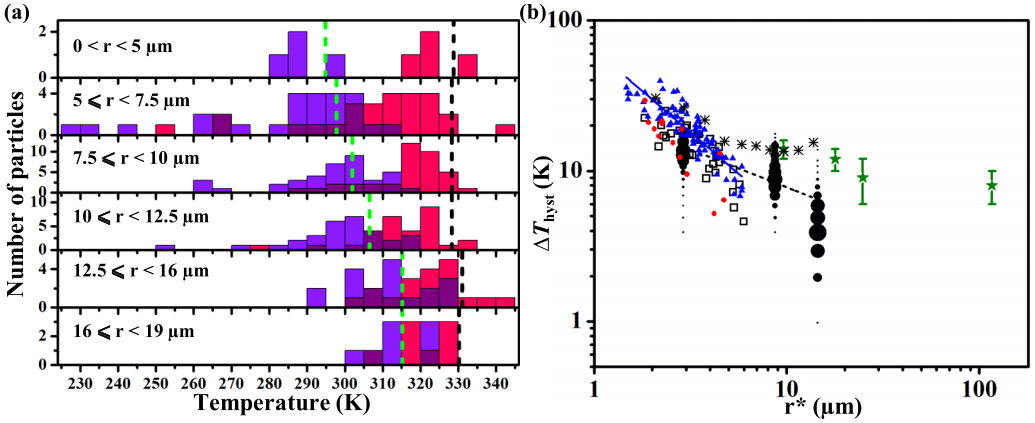

FIG. 8. (a) Overlapping histograms of the collected $(A_s + A_f)/2$ (red) and $(M_s + M_f)/2$ (blue) temperatures of 126 individual single-crystal particles from their $M(T)$ curves under 5 kOe, and the endothermic peak temperatures (black dashed line) and exothermic peak temperatures (green dashed line) of sieved alloy particles from DSC measurements; (b) the power law fit of ΔT_{hyst} on r^* (solid blue line) of $Ni_{43}Co_7Mn_{39}Sn_{11}$ alloy particles with gradual (blue triangle) transformations during cooling, and the power law fit of ΔT_{hyst} on r^* (black dashed line) of Ni-Mn-Sn alloy films (black circle) [16]. Hysteresis of $Ni_{43}Co_7Mn_{39}Sn_{11}$ alloy particles with hybrid (black square) and abrupt (red circle) transformations during cooling are plotted against r^*. Hysteresis of particle population by subtracting DSC exothermic peak temperatures from endothermic peak temperatures is plotted against r^* (asterisk). The size of the black circles shows different number of grains with the same hysteresis. The largest black circle represents number 66–78. The smallest black circle represents number 1–13. Green stars illustrate the hysteresis of Cu-Al-Ni microwires [15].

potentially remain trapped within particles at low temperatures which could spontaneously grow upon heating, negating the need to overcome a nucleation energy barrier at the beginning of the transformation from martensite to austenite.

In select cases, martensite to austenite phase transformation completes abruptly. This could be attributed to the instability in the energy-volume relationship at small volumes where interfacial energy terms dominate (Fig. 4). The distribution of particles with abrupt, hybrid, and gradual transformations does not show notable size dependence within each category [Fig. 8(b)]. In general, it is not surprising that particles with similar diameters show different transformation behavior, as the distribution of active nucleation sites, defect populations, and residual stresses are likely to vary dramatically across particles.

B. Model of size-dependent hysteresis

Statistical analysis of collected particle phase transformation temperatures and aggregate phase transformation temperatures of the particle population shows consistent size dependence of hysteresis. DSC was used to measure aggregate phase transformation temperatures of the 11 groups of sieved alloy particles with decreasing radii of this broader sample population (Fig. S5 [35]). The $(A_s + A_f)/2$ and $(M_s + M_f)/2$ temperatures of 126 individual single-crystal particles, $4.4 \leqslant r \leqslant 19.0\ \mu$m, were measured from their $\Delta M(T)$ curves, binned in six size increments, and compared with the corresponding DSC's endothermic and exothermic temperature peaks [Fig. 8(a)]. The distribution of $(M_s + M_f)/2$ temperatures shifts to lower temperatures with decreasing particle radius, while the endothermic peak temperature remains nearly constant. This behavior is consistent with our previous observation that in the smaller size fractions, particles are more likely to be nucleation limited during cooling than heating (Table I). During cooling, the possibility of including an active nucleation site decreases with decreasing particle volume, resulting in larger undercooling prior to martensite nucleation temperatures. However, residual austenite trapped within the particle at low temperatures could gradually grow upon heating, thereby eliminating the need for a nucleation event. Thus, the size effect on austenite transformation temperatures is insignificant over the measured ranges. With increasing particle radius, the hysteresis width of the particle population by DSC deviates slightly from the hysteresis of collected particles [Fig. 8(b)], potentially due to selecting only single-crystal particles from the sample population for magnetic measurements.

For $Ni_{43}Co_7Mn_{39}Sn_{11}$ alloy particles that showed gradual phase transformations during cooling, the size-dependent hysteresis is quantified by a power law model and attributed to friction-induced energy dissipation. In previous studies, power law models were used to describe size-dependent hysteresis in microscale Ni-Mn-Sn alloy films and Cu-Al-Ni microwires [Fig. 8(b)] [15,16]. With decreasing sample size and increasing ratios of sample surface area to volume, hysteresis increased by greater energy dissipation through enhanced frictional work during transformations [15,16]. In order to account for the effect of shape, we define a critical size r^* as the ratio of sample surface area to volume (for films, r^* = thickness; for wires, $r^* = r/2$; and for particles, $r^* = r/3$). The hysteresis of alloy particles is plotted against r^* [Fig. 8(b)], and the relation between hysteresis and r^* in alloy particles is quantified with a power law model ($\Delta T_{hyst} = ar^{*b}$, $a = 51.1 \pm 3.2$, $b = -0.9 \pm 0.1$) and explained by the pinning effect of defects at the surface of alloy particles [15]. The absolute value of the exponent parameter b of particles (0.9 ± 0.1) is larger than the value of Ni-Mn-Sn alloy films (0.3) due to different compositions and fabrication processes. Despite representing different alloy compositions and

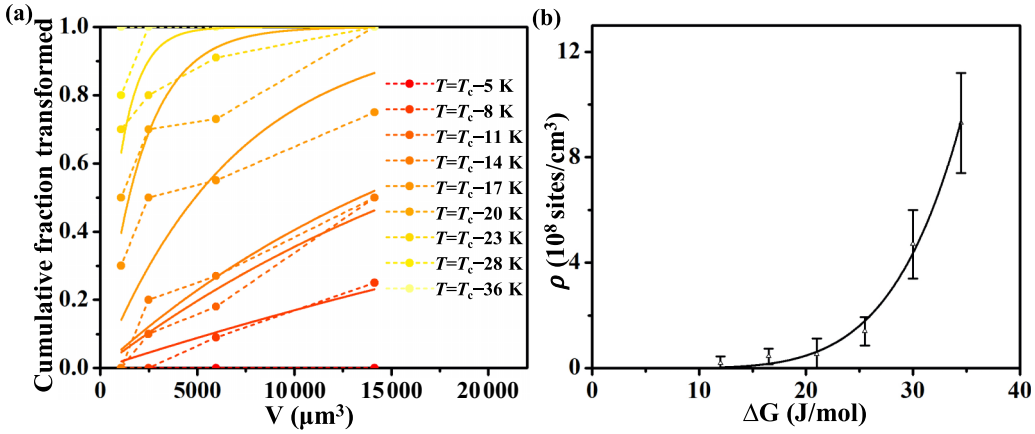

FIG. 9. (a) The cumulative fraction of transformation of $Ni_{43}Co_7Mn_{39}Sn_{11}$ particles with abrupt and hybrid transformations (circle connected by a dashed line) and the fitting of Eq. (1) (solid line) at given temperatures during cooling, V is the average particle volume in a group of particles; (b) the power law fit [$\rho = \alpha\ \Delta G^{\beta}$, $\alpha = 3.6 \pm 2.8$ (sites cm^{-3}), $\beta = 5.5 \pm 0.4$] of the density of active nucleation sites on ΔG during cooling.

sample geometries, size-dependent behavior, which describes increasing thermal hysteresis width with decreasing critical size, could be quantified by power law models in these small-scale multifunctional alloys ($r^* < 100\ \mu$m).

C. Nucleation-controlled hysteresis

With decreasing critical particle size and volume, the hysteresis of alloy particles with nucleation-limited transformations increases due to the lack of high-energy nucleation sites during martensitic transformations [Fig. 8(b)]. Nucleation site potency distributions of these alloy particles have been quantified as a function of thermodynamic driving force (ΔG) [13,42]. The cumulative fraction of transformation P, which presents the probability that a particle with volume V, contains at least one active nucleation site, is given by

$$P = 1 - \exp(-N) = 1 - \exp[-V\rho(\Delta G)], \qquad (1)$$

where N is the mean number of nucleation sites expected within a particle of volume V, ΔG is the excess driving force at a temperature below the equilibrium temperature (T_c) during cooling, and ρ is the density of active nucleation sites at a given ΔG.

Determination of an equilibrium temperature for a particular particle is a nontrivial problem as the equilibrium temperature of austenite and martensite phases of each particle are different due to different particle sizes, minor compositional variations, or different residual stress induced during processing. Furthermore, due to energetic barriers (of unknown magnitude) separating the stable and metastable phases, equilibrium temperature cannot be assessed directly. A linear correlation is shown between $(A_s + A_f)/2$ and $(M_s + M_f)/2$ temperatures of these alloy particles with nucleation-limited transformations (Fig. S6 [35]). Olson and Cohen have discussed the determination of T_c in four martensitic transformation models, including (1) behavior without friction ($T_c > A_f$), (2) elastic accommodation with two levels of frictional work (T_c approaches A_f), and (3) nonthermoelastic behavior resulting from plastic accommodation [$T_c \approx (M_s + A_f)/2$] [9,43,44]. The transformation behavior of our particles with abrupt and hybrid transformations is most consistent with the elastic accommodation model with frictional work. Thus, we adopt the use of A_f as the most reasonable approximation of T_c for each particle. In comparison, calculating by $T_c = (M_s + A_f)/2$ has the result of decreasing the equilibrium transformation temperature T_c, resulting in a calculated driving force ΔG approximately 52% that of the value presented here. Near equilibrium, $\Delta G = \Delta S(T_c - T)$ [42], where the entropy change of $Ni_{43}Co_7Mn_{39}Sn_{11}$ alloy particles is 188.2 kJ/(m^3 K) [45]. The collected alloy particles with abrupt and hybrid transformations during cooling are divided into four groups with decreasing particle radius (Fig. S7 [35]). The cumulative fraction of transformation P was calculated by the cumulative number fraction of transformed particles at a series of given temperatures during cooling: $T_c - 5$ K, $T_c - 8$ K, $T_c - 11$ K, $T_c - 14$ K, $T_c - 17$ K, $T_c - 20$ K, $T_c - 23$ K, $T_c - 28$ K, $T_c - 36$ K. Due to the T_c temperature of each particle being different, the given temperature of each particle is different. P was plotted against the average particle volume [Fig. 9(a)], after which ρ (sites/cm^3) was obtained by fitting Eq. (1) at a given temperature in Fig. 9(a), and was plotted against thermodynamic driving force (ΔG) in Fig. 9(b). Nucleation site potency distribution ρ was fit with a power law relationship [42,46]:

$$\rho = \alpha|\Delta G|^{\beta}, \qquad (2)$$

where α is a proportionality constant, β is an exponent, and ΔG is given in units of J/mol. Fitting parameters $\alpha = 3.6 \pm 2.8$ (sites cm^{-3}) and $\beta = 5.5 \pm 0.4$ were obtained.

Considering nucleation statistics across different classes of materials (Fig. 10), the nucleation site potency map could be divided into three parts according to the magnitude of thermal hysteresis width in the bulk material, $\Delta T_{hyst,bulk}$. For thermoelastic martensitic transformation particles with $\Delta T_{hyst,bulk} < 50$ K (or <20 K), the energy barrier of transformation is much smaller than the energy barrier of zirconia and Fe-Ni systems which both have large hysteresis or represent irreversible burst transformation [12,42,47–50]. For reversible thermoelastic martensitic transformation systems ($\Delta T_{hyst,bulk} < 50$ K), including nanoscale VO_2 precipitates,

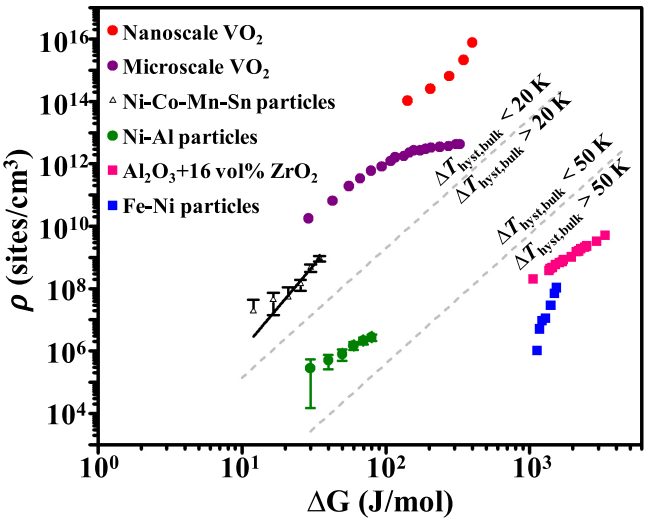

FIG. 10. Nucleation site potency distribution of nanoscale VO_2 particles [42], microscale VO_2 particles [47], microscale $Ni_{43}Co_7Mn_{39}Sn_{11}$ particles, Ni-Al particles [48], $Al_2O_3 + 16$ vol % ZrO_2 particles [49], and microscale Fe-Ni particles during cooling [12,13]. The black line shows the power law fit of the density of active nucleation sites on ΔG for $Ni_{43}Co_7Mn_{39}Sn_{11}$ particles.

hydrothermally synthesized microscale VO_2 particles ($V \leqslant 28.0\ \mu m^3$), microscale $Ni_{43}Co_7Mn_{39}Sn_{11}$ particles ($4.4 \leqslant r \leqslant 19.0\ \mu m$) fabricated by gas atomization, and Ni-Al particles ($50 \leqslant r \leqslant 250\ \mu m$), their nucleation site densities increased with similar tendency, which can be quantified by power law models [42,47,48]. The average β of the four power law models of nanoscale VO_2 precipitates, microscale VO_2 particles, $Ni_{43}Co_7Mn_{39}Sn_{11}$ particles, and Ni-Al particles is 4.1 ± 2.5. Thus, rather than a universal potency distribution relating the distribution of heterogeneous nucleation sites across different martensitic transformations, a correlation is observed between nucleation site potency distributions and the magnitude of the transformation hysteresis observed in the bulk alloy. This correlation is likely attributable to the larger elastic strain energy barrier in systems with large hysteresis, which also requires more potent defects to nucleate the transformation, while it seems likely that some difference in internal defect populations may also play a role in dictating nucleation potency distributions. These internal defect populations might be different due to different fabrication and thermal processing (e.g., thin film deposition vs metal droplets solidified), and can serve as active nucleation sites and affect martensitic transformation behavior.

V. CONCLUSIONS

Reversible thermoelastic martensitic transformations are observed in microscale $Ni_{43}Co_7Mn_{39}Sn_{11}$ particles. Magnetic measurements of 126 individual single-crystal particles are used. $\Delta M(T)$ curves of partial particles present gradual transformation processes (thermoelastic transformations) with size-dependent hysteresis, which is quantified by a power law model ($\Delta T_{hyst} = ar^{*b}$, $a = 51.1 \pm 3.2$, $b = -0.9 \pm 0.1$). The hysteresis of other particles with abrupt and hybrid transformations (nucleation-limited thermoelastic martensitic transformations) increases with reducing particle volume due to the low probability of including relatively sparse high-energy nucleation sites. Nucleation site potency distributions of these alloy particles are quantified [$\rho = \alpha \Delta G^{\beta}$, $\alpha = 3.6 \pm 2.8$ (sites cm^{-3}), $\beta = 5.5 \pm 0.4$] and compared against other martensitic transformation systems. For microscale $Ni_{43}Co_7Mn_{39}Sn_{11}$ particles ($4.4 \leqslant r \leqslant 19.0\ \mu m$), microscale VO_2 ($V \leqslant 28.0\ \mu m^3$), and nanoscale VO_2 with $\Delta T_{hyst,bulk} < 50$ K, nucleation site densities increase with similar tendency. The correlation between nucleation site potency distributions and the magnitude of the transformation hysteresis observed in the bulk alloy is likely attributed to the magnitude of the elastic strain energy barrier.

The datasets generated and analyzed during the current study are available from the corresponding author on reasonable request. All data generated or analyzed during this study are included in this published article and the Supplemental Material [35].

ACKNOWLEDGMENTS

This material is based upon work supported by the National Science Foundation under Grant No. 1847956. I.K. would like to acknowledge the financial support of the National Science Foundation through Grant No. 1905325.

The authors declare no competing interests.

[1] S.-H. Song, J.-Y. Lee, H. Rodrigue, I.-S. Choi, Y. J. Kang, and S.-H. Ahn, Sci. Rep. **6**, 21118 (2016).
[2] H. Ossmer, C. Chluba, S. Kauffmann-Weiss, E. Quandt, and M. Kohl, APL Mater. **4**, 064102 (2016).
[3] H. Ossmer, F. Wendler, M. Gueltig, F. Lambrecht, S. Miyazaki, and M. Kohl, Smart Mater. Struct. **25**, 085037 (2016).
[4] S. Fähler, U.K. Rößler, O. Kastner, J. Eckert, G. Eggeler, H. Emmerich, P. Entel, S. Müller, E. Quandt, and K. Albe, Adv. Eng. Mater. **14**, 10 (2012).
[5] J. San Juan, M. L. Nó, and C. A. Schuh, Nat. Nanotechnol. **4**, 415 (2009).
[6] M. Kabla, E. Ben-David, and D. Shilo, Smart Mater. Struct. **25**, 075020 (2016).
[7] A. Diestel, P. Chekhonin, R. Niemann, W. Skrotzki, K. Nielsch, and S. Fähler, Phys. Status Solidi B **255**, 1700330 (2018).
[8] P. J. S. Buenconsejo, R. Zarnetta, M. Young, H. Brunken, A. Mehta, and A. Ludwig, Thin Solid Films **564**, 79 (2014).
[9] J. Ortin and A. Planes, Acta Metall. **36**, 1873 (1988).
[10] H. Tong and C. Wayman, Acta Metall. **23**, 209 (1975).
[11] E. S. Machlin and M. Cohen, JOM **3**, 746 (1951).
[12] R. E. Cech and D. Turnbull, JOM **8**, 124 (1956).
[13] G. Olson, K. Tsuzaki, and M. Cohen, Mater. Res. Soc. Symp. Proc. **57**, 129 (1985).
[14] C. Magee, Metall. Trans. **2**, 2419 (1971).
[15] Y. Chen and C. A. Schuh, Acta Mater. **59**, 537 (2011).

[16] Y. Zhang, J. Billman, and P. J. Shamberger, Acta Mater. **180**, 116 (2019).
[17] G. Sure and L. Brown, Metall. Mater. Trans. A **15**, 1613 (1984).
[18] S. Montecinos, A. Cuniberti, and A. Sepúlveda, Mater. Charact. **59**, 117 (2008).
[19] I. Dvorak and E. Hawbolt, Metall. Trans. A **6**, 95 (1975).
[20] Y. Sutou, T. Omori, K. Yamauchi, N. Ono, R. Kainuma, and K. Ishida, Acta Mater. **53**, 4121 (2005).
[21] D. N. Adnyana, Metallography **19**, 187 (1986).
[22] Z. Zhang, X. Ding, J. Sun, T. Suzuki, T. Lookman, K. Otsuka, and X. Ren, Phys. Rev. Lett. **111**, 145701 (2013).
[23] N. Ozdemir, I. Karaman, N. Mara, Y. I. Chumlyakov, and H. Karaca, Acta Mater. **60**, 5670 (2012).
[24] J. San Juan and M. Nó, J. Alloys Compd. **577**, S25 (2013).
[25] J. San Juan, M. L. Nó, and C. A. Schuh, Adv. Mater. **20**, 272 (2008).
[26] T. Waitz, V. Kazykhanov, and H. Karnthaler, Acta Mater. **52**, 137 (2004).
[27] Y. Q. Fu, S. Zhang, M. Wu, W. M. Huang, H. Du, J. Luo, A. Flewitt, and W. Milne, Thin Solid Films **515**, 80 (2006).
[28] G. Olson and M. Cohen, Metall. Trans. A **6**, 791 (1975).
[29] P. L. Mangonon and G. Thomas, Metall. Trans. **1**, 1577 (1970).
[30] R. Lagneborgj, Acta Metall. **12**, 823 (1964).
[31] S. Dash and N. Brown, Acta Metall. **14**, 595 (1966).
[32] T. Saburi, T. Komatsu, S. Nenno, and Y. Watanabe, J. Less-Common Met. **118**, 217 (1986).
[33] P. Ferraglio and K. Mukherjee, Acta Metall. **22**, 835 (1974).
[34] N. Barta and I. Karaman, Mater. Sci. Eng. A **751**, 201 (2019).
[35] See Supplemental Material at http://link.aps.org/supplemental/10.1103/PhysRevMaterials.5.023401 for $\Delta M(T)$ curves of alloy particles. DSC measurements of Ni-Co-Mn-Sn particles and the linear fit of $(A_s + A_f)/2$ on $(M_s + M_f)/2$ temperatures of alloy particles are also included.
[36] R. Modak, M. M. Raja, and A. Srinivasan, J. Magn. Magn. Mater. **448**, 146 (2018).
[37] R. Kainuma, Y. Imano, W. Ito, Y. Sutou, H. Morito, S. Okamoto, O. Kitakami, K. Oikawa, A. Fujita, and T. Kanomata, Nature **439**, 957 (2006).
[38] S. Aksoy, M. Acet, P. P. Deen, L. Mañosa, and A. Planes, Phys. Rev. B **79**, 212401 (2009).
[39] K. Ollefs, C. Schöppner, I. Titov, R. Meckenstock, F. Wilhelm, A. Rogalev, J. Liu, O. Gutfleisch, M. Farle, H. Wende, and M. Acet, Phys. Rev. B **92**, 224429 (2015).
[40] K. Otsuka, H. Sakamoto, and K. Shimizu, Acta Metall. **27**, 585 (1979).
[41] J. San Juan, M. Nó, and C. Schuh, Acta Mater. **60**, 4093 (2012).
[42] R. Lopez, T. E. Haynes, L. A. Boatner, L. C. Feldman, and R. F. Haglund, Jr., Phys. Rev. B **65**, 224113 (2002).
[43] G. Olson and M. Cohen, Scr. Metall. **11**, 345 (1977).
[44] G. Olson and M. Cohen, Scr. Metall. **9**, 1247 (1975).
[45] K. Ito, W. Ito, R. Y. Umetsu, I. Karaman, K. Ishida, and R. Kainuma, Mater. Trans. **52**, 2270 (2011).
[46] I.-W. Chen, Y. Chiao, and K. Tsuzaki, Acta Metall. **33**, 1847 (1985).
[47] H. Clarke, B. D. Caraway, D. G. Sellers, E. J. Braham, S. Banerjee, R. Arróyave, and P. J. Shamberger, Phys. Rev. Mater. **2**, 103402 (2018).
[48] S. Rubini, C. Dimitropoulos, and F. Borsa, Phys. Rev. B **49**, 9331 (1994).
[49] A. Heuer, N. Claussen, W. M. Kriven, and M. Ruhle, J. Am. Ceram. Soc. **65**, 642 (1982).
[50] M. Hayakawa and M. Tamaki, Mater. Trans. **49**, 1785 (2008).